AIAA JOURNAL
Vol. 45, No. 10, October 2007

Numerical Investigation of Plasma-Based Flow Control for Transitional Highly Loaded Low-Pressure Turbine

Donald P. Rizzetta* and Miguel R. Visbal†
U.S. Air Force Research Laboratory, Wright–Patterson Air Force Base, Ohio 45433-7512

DOI: 10.2514/1.29602

Plasma-based active flow control was simulated numerically for the subsonic flow through a highly loaded low-pressure turbine. The configuration corresponded to previous experiments and computations which considered flow at a Reynolds number of 25,000 based upon axial chord and inlet conditions. In this situation, massive separation occurs on the suction surface of each blade due to uncovered turning. The present exploratory numerical study was performed to investigate the use of asymmetric dielectric–barrier–discharge actuators for mitigating separation, thereby decreasing turbine wake losses and increasing efficiency. Solutions were obtained for the Navier–Stokes equations, which were augmented by a phenomenological model that was used to represent plasma-induced body forces imparted by the actuator on the fluid. The numerical method used a high-fidelity time-implicit scheme, employing domain decomposition to carry out calculations on a parallel computing platform. A high-order overset grid approach preserved spatial accuracy in a locally refined embedded region. The magnitude of the plasma-induced body force required for control is examined, and both continuous and pulse-modulated actuations are considered. Novel use of counterflow actuation is also investigated, and the effects of pulsing frequency and duty cycle are considered. Features of the flowfields are described, and resultant solutions are compared with each other, with previous mass-injection control cases, and with the baseline situation where no control was enforced.

Nomenclature

A = plasma force amplitude
C_p = time–mean pressure coefficient, $2(\bar{p} - \bar{p}_i)/\rho_i \bar{q}_i^2$
c = turbine blade axial chord
D_c = plasma scale parameter
$\boldsymbol{E}$ = nondimensional electric field vector
E_{k_z}, E_ω = nondimensional turbulent kinetic energy wave number and frequency spectra
f = dimensional imposed actuator pulsing frequency, Hz
I, J, K = coordinate grid indices in the circumferential, blade normal, and spanwise directions
k_z = nondimensional spanwise wave number
l, n = nondimensional blade tangential and normal directions
M = Mach number
P_t = nondimensional total pressure
p = nondimensional static pressure
q = nondimensional planar velocity magnitude, $\sqrt{u^2 + v^2}$
q_c = nondimensional charge density
Re = chord inlet Reynolds number, $\rho_i \bar{q}_i Re_\infty / \mu_i$
Re_∞ = reference Reynolds number, $\rho_\infty q_\infty c / \mu_\infty$
s = nondimensional spanwise domain extent
t = nondimensional time based upon the reference velocity u_∞ and the chord c
u, v, w = nondimensional Cartesian velocity components in the x, y, z directions
x, y, z = nondimensional Cartesian coordinates in the streamwise, vertical, and spanwise directions
$\Delta l^+, \Delta n^+, \Delta z^+$ = nondimensional mesh spacings in blade tangential, normal, and spanwise directions given in law-of-the-wall units
ξ, η, ζ = nondimensional body-fitted computational coordinates
ω = nondimensional frequency

Subscripts

i, o = inflow and outflow conditions
min, max = minimum and maximum values
∞ = dimensional reference value

Superscripts

$\bar{\ }$ = time–mean quantity
$'$ = root-mean-square fluctuating component

I. Introduction

LOW-PRESSURE turbines are commonly used in the propulsion systems of unmanned air vehicles (UAVs) employed for reconnaissance and combat purposes. Because of a reduction in atmospheric density during high-altitude cruise, such low-pressure turbines may encounter Reynolds numbers, based upon blade axial chord and inlet conditions, below 25,000. In this situation, boundary layers along a large extent of blade surfaces can remain laminar, even in the presence of elevated freestream turbulence levels. The laminar boundary layers are then particularly susceptible to flow separation over the aft portion of blade suction surfaces, causing blockage in flow passages and a significant reduction in turbine efficiency.

Recent experiments of low-pressure turbines [1] have investigated the feasibility of increasing the interblade spacing, thereby raising the per blade loading. For practical applications, a higher loading can reduce the turbine part count and stage weight. Increased blade spacing, however, is accompanied by more extensive boundary-layer separation on the suction surface of each blade due to uncovered turning, resulting in a further reduction of efficiency and

---

Presented as Paper 938 at the 45th AIAA Aerospace Sciences Meeting and Exhibit, Reno, NV, 8–11 January 2007; received 5 January 2007; revision received 27 February 2007; accepted for publication 5 April 2007.

*Senior Research Aerospace Engineer, Computational Sciences Branch, AFRL/VAAC. Associate Fellow AIAA.

†Technical Area Leader, Computational Sciences Branch, AFRL/VAAC. Associate Fellow AIAA.

additional wake losses. Unless these adverse circumstances for highly loaded low-pressure turbines can be overcome, ceiling limitations may be imposed for prolonged UAV operations.

A number of experimental investigations by Bons et al. [2–4] and by Sondergaard et al. [1,5] have explored the use of both steady and pulsed vortex generator jets, which may be actuated upon demand, as a means of flow control in low-pressure turbines. When installed, these devices can remain idle at sea level where flow along the blades is attached and activated at altitude when separation occurs. Extensive measurements verified that vortex generator jets dramatically reduced separation, resulting in decreased losses and increased efficiency. As an alternative to vortex-generating jets, other experiments have considered the use of plasma-based actuators for controlling turbine flowfields [6–10]. In addition to the absence of more complex mechanical or pneumatic systems, such devices have relatively low power requirements and can operate over a broad range of frequencies. Plasma actuation has also been considered in a number of other experimental studies including rotorcraft blade control [11], lift enhancement for stationary and oscillating airfoils [12–14], plasma flaps and slats [15], dynamic stall [16], tip clearances in turbine blades [17], bluff-body flows [18], and aerodynamic control of UAVs [19].

Advances in the speed and storage capacity of high-performance computing systems have allowed numerical simulation to emerge as a viable means for the investigation of flows through low-pressure turbines [20–29]. Computational studies have also been performed for the use of plasma-based actuators in flow-control applications. Because these problems are typically characterized by transitional and turbulent flowfields, high-fidelity time-accurate three-dimensional approaches are required to properly account for the physical processes inherent in their description. Specification of plasma effects derived from fundamental principles is therefore computationally prohibitive. Thus, numerical simulations primarily have relied upon approximate procedures to represent plasma-induced body forces imparted by the actuator on the fluid field. A “loosely coupled” approach, combining two separate computations, was used for plasma control of a wing stall [30]. The somewhat less basic technique incorporating a simplified phenomenological model has been more widely employed and resulted in calculations for the control of wing sections [31], delta wings [32], wall-bounded flows [30], and other configurations.

Dielectric–barrier–discharge (DBD) actuators typically operate in the low radio frequency range (1–10 kHz) with voltage amplitudes of 5–10 kV. Experimental measurements indicate that time-averaged plasma-induced body forces generated by DBD devices are the dominant mechanism for exerting control. An overview of the design, optimization, and application of these actuators has been given by Corke and Post [8]. The present investigation provides companion simulations to both previous experiments and computations of plasma-based flow-control applications. The specific situation explores the use of a single asymmetric DBD actuator to mitigate separation on the suction surface of a highly loaded low-pressure turbine.

The turbine blade geometry considered in the present study corresponds to plasma-control experiments of Huang et al. [7,10]. But because the interblade spacing employed in the current investigation is greater than that used by Huang et al. [7,10], no comparison with measured data is possible. The configuration, however, is identical to that of previous simulations for vortex-generating jet control of turbines [28,29], so that the two situations may be contrasted directly. This effort is focused on the identification of effective strategies for separation control of highly loaded low-pressure turbines. The magnitude of the plasma-induced body force required for such control is examined, and both continuous and pulse-modulated actuation are simulated. Novel use of counterflow actuation, which was first proposed by Visbal et al. [30], is also investigated, and the effects of pulsing frequency and duty cycle are considered. Resultant solutions are compared with each other, with previous mass-injection control cases and with the baseline situation where no control was enforced.

II. Governing Equations and Numerical Method

The governing fluid equations are taken as the unsteady three-dimensional compressible unfiltered Navier–Stokes equations. After introducing a curvilinear coordinate transformation to a body-fitted system, the equations are cast in the following nondimensional conservative form:

$$\frac{\partial}{\partial t}\left(\frac{1}{\mathcal{J}}\boldsymbol{Q}\right)+\frac{\partial}{\partial\xi}\left(\boldsymbol{F}-\frac{1}{Re_\infty}\boldsymbol{F}_v\right)+\frac{\partial}{\partial\eta}\left(\boldsymbol{G}-\frac{1}{Re_\infty}\boldsymbol{G}_v\right)+\frac{\partial}{\partial\zeta}\left(\boldsymbol{H}-\frac{1}{Re_\infty}\boldsymbol{H}_v\right)=D_c q_c \boldsymbol{S} \tag{1}$$

Here t is the time, ξ, η, ζ the computational coordinates, $\boldsymbol{Q}$ the vector of dependent variables, $\boldsymbol{F}, \boldsymbol{G}, \boldsymbol{H}$ the inviscid flux vectors, $\boldsymbol{F}_v, \boldsymbol{G}_v, \boldsymbol{H}_v$ the viscous flux vectors, and $\boldsymbol{S}$ the source vector representing the effect of plasma-induced body forces.

Time-accurate solutions to Eq. (1) are obtained numerically by the implicit approximately factored finite-difference algorithm of Beam and Warming [33] employing Newton-like subiterations [34], which has evolved as an efficient tool for generating solutions to a wide variety of complex fluid flow problems. Second-order-accurate backward-implicit time differencing was used to obtain temporal derivatives.

The implicit segment of the algorithm incorporates second-order-accurate centered differencing for all spatial derivatives, and uses nonlinear artificial dissipation [35] to augment stability. Efficiency is enhanced by solving this implicit portion of the factorized equations in diagonalized form [36]. Temporal accuracy, which can be degraded by use of the diagonal form, is maintained by using subiterations within a time step. This technique has been commonly invoked to reduce errors due to factorization, linearization, diagonalization, and explicit application of boundary conditions. It is useful for achieving temporal accuracy on overset zonal mesh systems, and for a domain decomposition implementation on parallel computing platforms. Any deterioration of the solution caused by use of artificial dissipation and by lower-order spatial resolution of implicit operators is also reduced by the procedure. Three subiterations per time step have been applied to preserve second-order temporal accuracy in the present application.

The compact difference scheme which is employed to evaluate spatial derivatives for the explicit part of the factored form of Eq. (1) is based upon the pentadiagonal system of Lele [37], and is capable of attaining spectral-like resolution. This is achieved through the use of a centered implicit difference operator with a compact stencil, thereby reducing the associated discretization error. For the present computations, a fourth-order tridiagonal subset of Lele’s system is used. The scheme has been adapted by Visbal and Gaitonde [38] as an implicit iterative time-marching technique, applicable for unsteady vortical flows. It is used in conjunction with a sixth-order low-pass Pade-type nondispersive spatial filter developed by Gaitonde et al. [39], which has been shown to be superior to the use of explicitly added artificial dissipation for maintaining both stability and accuracy on stretched curvilinear meshes [38]. The filter is applied to the solution vector sequentially in each of the three computational directions following each subiteration. A more thorough description of the governing equations and complete details of the numerical method appear in [40], but have been omitted here for brevity. Application of the subiteration process and use of the high-order filter scheme results in solutions with fourth-order spatial and second-order temporal accuracy.

The aforementioned features of the numerical algorithm are embodied in a parallel version of the time-accurate three-dimensional computer code FDL3DI [41], which has proven to be reliable for steady and unsteady fluid flow problems, including the simulation of flows over delta wings with leading-edge vortices [42–44], vortex breakdown [43,44], direct numerical simulation of transitional wall jets [45] and synthetic jet actuators [46], and direct numerical and large-eddy simulation of subsonic [23,29,47,48] and supersonic flowfields [49–51].

III. Plasma Model

Many quantitative aspects of the fundamental processes governing plasma/fluid interactions remain unknown or computationally prohibitive, particularly for transitional and turbulent flows. These circumstances have given rise to the development of a wide spectrum of models with varying degrees of sophistication that may be employed for more practical simulations. Among the simplified methods focused specifically on discharge/fluid coupling is that of Roth et al. [52,53], who associated the transfer of momentum from ions to neutral particles based upon the gradient of electric pressure. A more refined approach, suitable for coupling with fluid response was proposed by Shyy et al. [54], using separate estimates for the charge distribution and electric field. Known plasma physics parameters were linked to experimental data. This model has been successfully employed for several previous simulations of plasma-controlled flows [30–32] and is also adopted in the present investigation.

A schematic representation of a typical single asymmetric DBD plasma actuator is depicted in Fig. 1. The actuator consists of two electrodes that are separated by a thin dielectric insulator and mounted on the turbine blade surface. An oscillating voltage, in the kHz frequency range, is applied to the electrodes, developing an electric field about the actuator. When the imposed voltage is sufficiently high, the dielectric produces a barrier discharge that weakly ionizes the surrounding gas. Momentum acquired by the charged particles arising from the electric field is transferred to the primary neutral molecules by collisional interactions. The temporal and spatial evolution of the particle distribution and the resulting electrostatic force field are not well understood nor easily predicted. In the numerical exploration of flow-control strategies, the entire process may be modeled as a body force vector acting on the net fluid external to the actuator, which produces a flow velocity.

The model for the geometric extent of the plasma field generated by such an actuator is indicated in Fig. 2. The triangular region defined by the line segments AB, CA, and CB constitutes the plasma boundary. Outside of this region it is assumed that the electric field is not strong enough to ionize the air. The electric field has its maximum value on segment CB and varies linearly within ABC. The peak value of the electric field is obtained from the applied voltage and the spacing between the electrodes. Along the segment AB, the electric field diminishes to its threshold value, which was taken as 30 kV/cm, in accordance with the Shyy et al. [54] model. The electric body force is equal to $q_c \boldsymbol{E}$ and provides coupling from the plasma to the fluid, resulting in the source vector $\boldsymbol{S}$ appearing in Eq. (1). It is assumed that this force acts locally tangential to the blade surface. Because the charge density is assumed to be constant within the region ABC [54], its nondimensional representation q_c is taken as unity, corresponding to the value of 1.0×10^{11} electrons/cm^3 [54]. The plasma scale parameter D_c arises from nondimensionalization of the governing equations, and represents the ratio of the electrical force of the plasma to the inertial force of the fluid, and is defined as

$$D_c = \frac{\rho_c e_c \mathcal{E}_r c}{\rho_\infty u_\infty^2} \tag{2}$$

where $\rho_c = 1.0 \times 10^{11}$ electrons/cm^3, $e_c = 1.6 \times 10^{-19}$ coulomb, and $\mathcal{E}_r$ is a reference electric field magnitude.

Some specific details of the plasma model which were incorporated in the present simulations were specified corresponding to the turbine blade experiments of Huang et al. [7,9,10]. The ratio of the threshold electric field magnitude to its peak value was taken as 0.043. Referring to Fig. 2, the distances CA and CB nondimensionalized by the blade chord were specified as $CA = 0.0125$ and $CB = 0.0250$. These values are similar to those employed in previous simulations for winglike configurations [30–32]. For the purposes of these simulations, it is assumed that the actuator is mounted flush with the turbine blade surface and does not protrude above it. Because of empiricism of the plasma model, there is some ambiguity regarding the value of the scale parameter D_c. In this investigation, its amplitude is varied in order to study the effect of the plasma strength on the turbine blade flowfield. It should be noted that the electric field is not altered during variation of the scale parameter D_c. Another unresolved issue regarding the model is the direction of the force imposed on the flowfield. Here, we assume a component only in the positive or negative x direction (approximately tangent to the blade surface), resulting in formation of a coflowing or counterflowing fluid velocity, respectively. This representation appears to be consistent with experimental observations of plasma-actuator flowfields. Moreover, the work of Gaitonde et al. [31] has shown that if the plasma force is predominantly tangential to the solid surface, the resulting control is not sensitive to its exact direction.

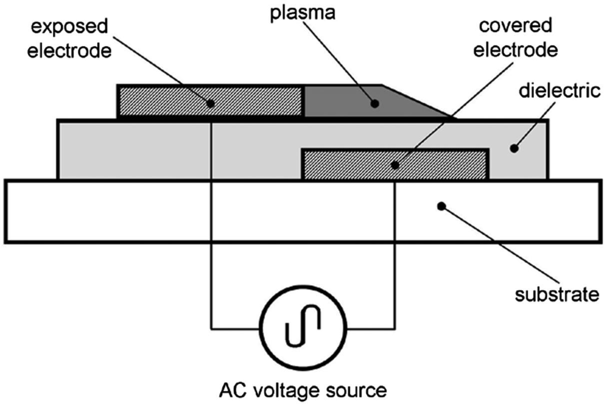

Fig. 1 Schematic representation of plasma actuator.

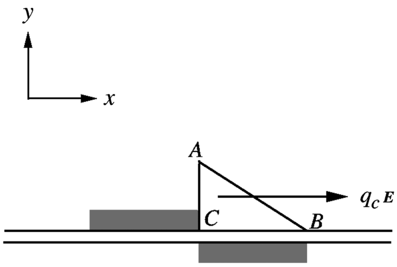

Fig. 2 Geometry for plasma model.

IV. Details of the Computations

Shown in Fig. 3 is a schematic representation of the turbine blade shape, given by the Pratt and Whitney "PakB" research design, which is a Mach number scaled version of geometries typically used in highly loaded low-pressure turbines [1–5]. This blade geometry has an inlet flow angle $\alpha_i = 35.0$ deg and a design exit flow angle $\alpha_o = 60.0$ deg. The chord normalized interblade spacing $b = 4/3$ corresponds to a solidity (chord/spacing) of 0.75.

A. Computational Meshes

To conserve computational resources, only a single turbine blade passage is considered, and periodic conditions are enforced in the

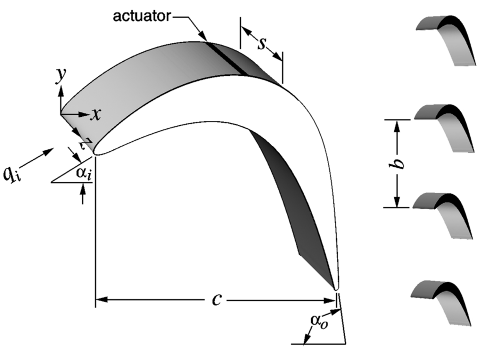

Fig. 3 Schematic representation of the turbine blade configuration.

vertical direction (y) to represent a single turbine stage flowfield. The computational domain surrounding the blade was described by a body-fitted mesh system, whose origin was located at the inboard leading edge of the blade (see Fig. 3). The mesh employs an O-grid topology and was elliptically generated using automated software [55]. Figure 4a indicates the basic grid about the turbine blade, which was composed of 348 points in the circumferential direction (I), 189 points in the blade normal direction (J), and 101 points in the spanwise direction (K). Minimum spacing in the J direction occurs at the blade surface. Mesh points for $1 \leq I \leq 5$ and $I_{\max-4} \leq I \leq I_{\max}$ are coincident in an overlap region at the blade leading edge so that periodic conditions in the circumferential direction may be enforced to complete the O-grid construct. To accommodate periodic conditions in the vertical direction, the streamwise (x) point locations and vertical spacing along $I_{1u} - I_{2u}$ are identical to that along $I_{1l} - I_{2l}$ for $J_{\max-4} \leq J \leq J_{\max}$.

To properly capture the correct fluid physics for the flow-control cases, the basic grid structure was modified to enhance resolution in the actuator and near-wall regions. This was done by removing points in the near-wall grid, indicated by the blanked area of Fig. 4a, and replacing them with an embedded refined mesh as seen in Fig. 4b. This technique is identical to that which was successfully employed by Rizzetta and Visbal [29] in a similar computation. The size of the refined-mesh region was ($313 \times 185 \times 101$) grid points in ($I, J, K$), respectively.

To facilitate application of inflow and outflow conditions to the turbine blade domain, overset grids were used upstream and downstream of the blade region. These are found in Fig. 4c and consisted of ($46 \times 61 \times 101$) and ($31 \times 75 \times 101$) mesh points in the streamwise, vertical, and spanwise directions for the upstream and downstream domains, respectively. Half of the grid points in the vertical direction are seen in the figure. The spanwise extent of the computational domain s was taken as 0.2. This value was found to be adequate to capture the transitional flowfield in the prior investigation of Rizzetta and Visbal [23]. The grid refinement study for the baseline case of [29] indicates that adequate resolution should be achieved for the present computations.

For coflowing control, the actuator was located at $x = 0.37$, corresponding to the time–mean separation point for the baseline case. This is identical to the position of vortex-generating jets in previous mass-injection simulations [28,29]. With counterflow control, it is believed to be beneficial to initiate actuation upstream of the separation. In this case then, the actuator is located at $x = 0.34$. For all situations, the actuator extends across the entire span of the blade, which is consistent with plasma-control turbine blade experiments [7,9].

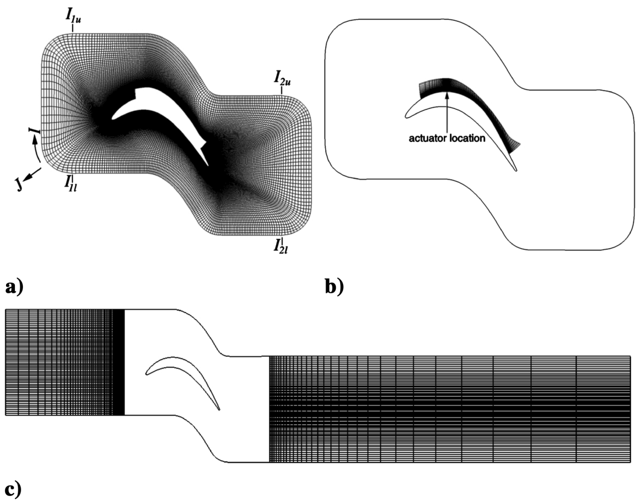

Fig. 4 Turbine blade computational mesh system.

B. Boundary Conditions

Inflow and outflow conditions for the complete turbine blade domain were obtained in a manner consistent with subsonic internal flows, which have commonly been employed in Reynolds-averaged Navier–Stokes (RANS) applications [56]. Along the upstream boundary the total pressure, total temperature, and inlet flow angle were specified, and the velocity magnitude was obtained from the interior solution. Downstream, the exit static pressure (p_∞) was fixed, and other flow variables were extrapolated from within the domain. Because the inflow velocity develops as part of the solution, the Reynolds number based upon the inflow conditions was not known a priori. A reference Mach number (M_∞) of 0.1 was selected for all computations. For the baseline solution, the reference Reynolds number (Re_∞) was adjusted to match the desired inflow condition, Re. This same Reynolds number was then employed in all subsequent simulations. When flow control was applied, however, the inflow velocity magnitude increased due to a reduction of blockage in the blade passage. Although this situation was anticipated, the reference Reynolds number was not altered. Thus, the inflow Reynolds numbers are somewhat higher than the nominal value of 25,000. This approach for the inflow and outflow boundaries was previously employed by Rizzetta and Visbal [23,28,29] in similar computations.

Periodic conditions were applied along the upper and lower portions of the turbine blade as indicated previously in Fig. 4a. Periodic conditions were also applied along upper and lower horizontal boundaries of the upstream and downstream domains seen in Fig. 4c. The downstream domain was intensionally severely stretched in the streamwise direction to reduce spurious reflections from the outflow boundary. This technique transfers information to high spatial wave numbers and then dissipates it by the low-pass filter [57]. Flow variables in all regions of overlapped meshes were obtained from explicit sixth-order accurate Lagrangian interpolation formulas. This includes the upstream and downstream domains, the turbine blade grid, and the refined-mesh region. The interpolation approach for high-order numerical solutions has been successfully applied by Sherer [58] for the simulation of fluid dynamic and acoustic problems. As stated previously, periodic conditions were invoked in the spanwise direction. On the blade surface, the no-slip condition was enforced along with an isothermal wall, and a fourth-order accurate representation of zero normal pressure gradient.

C. Temporal Considerations

Operationally, DBD actuators are inherently unsteady devices. Within the context of the phenomenological model, however, the body force imposed on the fluid is assumed to be steady, owing to the high frequency of the applied voltage (typically 5–10 kHz). In results to follow, this steady-force situation will be referred to as continuous powered actuation. These devices may also be operated in a pulsed manner as described by Corke and Post [8], thereby reducing total power consumption. The pulsed mode of operation also introduces low-frequency forcing to the flow, which may be more receptive to control, and offers the potential of improved effectiveness. For simulation of pulsed actuation, the forcing amplitude is modulated according to the duty cycle illustrated in Fig. 5. Here, t_d is the portion of the fundamental period t_p over which the device is active. The ratio $t_d/t_p \times 100$ expressed as a percentage is commonly referred to as the duty cycle d. A duty cycle of $d = 50\%$ is depicted in Fig. 5, but cycles of both 25 and 50% are explored in this study. The amplitude time history for one cycle appearing in the figure consists of a series of piecewise continuous cubic and linear functions which were used to represent the pulsing duration. This description is identical to that used in previous mass-injection control simulations [28,29]. It should be noted that the applied waveform introduces multiple harmonics of the primary frequency as demonstrated in [29,30].

The basic nondimensional forcing frequency $f^+ = 7.56$ is identical to that of previous experiments [2–5] and simulations [28,29] with

$$f^+ = cf/u_\infty \bar{q}_i \tag{3}$$

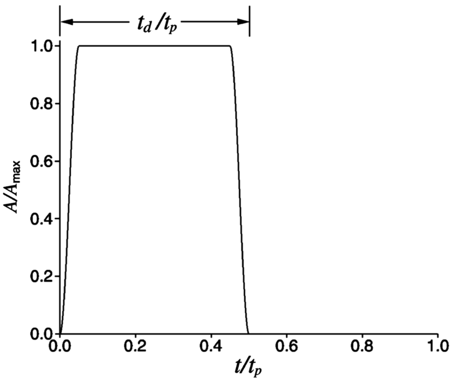

Fig. 5 Plasma force amplitude time history.

Most pulsed simulations were performed at the basic frequency, but one computation was carried out at one-half the basic value ($f^+ = 3.78$). Calculations were obtained using a time step of $\Delta t = 1.5 \times 10^{-4}$, where t is nondimensionalized by reference quantities. For pulsed cases, the unsteady period was described by 1300 and 2600 time steps/cycle for $f^+ = 7.56$ and 3.78, respectively. Flowfields for each case were initialized from previously obtained solutions and processed for 104,000 time steps in order to remove transients. During this period, the inflow velocity and trailing-edge pressure were monitored to determine when an equilibrium state was attained. Final results were then evolved for an additional 104,000 steps during which statistical information was collected. Statistics were monitored to assure that a converged sample was achieved. This duration represents approximately 11.9 characteristic time units based upon the inflow velocity and corresponds to 80 ($f^+ = 7.56$) or 40 ($f^+ = 3.78$) cycles for pulsed control.

D. Domain Decomposition

For parallel processing, the previously described computational domains were decomposed into a series of subzones, which were then distributed on individual processors of a massively parallel computing platform (IBM SP4+, HP XC Opteron). Decompositions were constructed to provide an approximately equal number of grid points in every subzone, thereby balancing the computational work load among the processors. Faces at the boundaries of each subzone block were overset into adjacent domains, such that an overlap of five planes was established. Although this incurred an overhead due to redundant computation, it maintained the formal high-order accuracy of both the numerical differencing and filtering schemes. Because a vast majority of the overlapping mesh points of the respective decompositions were coincident, no further interpolation was required. Automated software [59] was used to identify donor and recipient grid points in the overlapping domains. Internode communication among the processors was established through standard message-passing interface (MPI) library routines [60], which were used to transfer information between the various subzones of the flowfield at domain boundaries. A total of 176 processors were employed for all of the computations reported here.

V. Overview of the Simulations

Because of ambiguity in the choice of the scale parameter D_c, preliminary results were obtained in two spatial dimensions, neglecting the spanwise direction. It was realized that these simulations could not correctly represent the transitional turbine blade flowfield, but they were used to guide the computationally intensive three-dimensional calculations. A parametric study revealed that the time–mean flow could remain attached along the entire blade suction surface using continuous plasma actuation with $D_c = 650.0$. Fully three-dimensional computations were then performed for $D_c = 650.0$. Although this value is considerably smaller than that used in the previous simulation for a wing section [31] ($D_c = 2400.0$), it still may not represent a realistically achievable level of plasma actuation. Thus, results were also obtained for $D_c = 75.0$, a value believed to be attainable by current plasma devices. In a effort to explore techniques having even lower power requirements, coflow and counterflow actuation with $D_c = 25.0$ were then considered. For comparison, the value of D_c corresponding to the experiments of Huang et al. [7,9,10] was estimated to be 23.4.

Three-dimensional simulations were carried out for 10 specific cases, which are summarized in Table 1. These included continuous and pulsed coflow actuation for $D_c = 650.0$ and $D_c = 75.0$, as well as continuous and pulsed actuation with coflow and counterflow control for $D_c = 25.0$. Also provided in the table are results for the previously obtained baseline case without flow control, and cases which employed steady and pulsed vortex-generating jets [28]. From the time–mean flowfields, control effectiveness may be quantified by calculation of the integrated wake total pressure loss coefficient C_w, defined as

$$C_w = \frac{1}{s(y_{\max} - y_{\min})} \int_0^s \int_{y_{\min}}^{y_{\max}} \left(\frac{P_{ti} - \bar{P}_{to}}{P_{ti} - \bar{p}_i} \right) \mathrm{d}y \, \mathrm{d}z \qquad (4)$$

Equation (4) is evaluated along the upstream boundary of the downstream mesh in Fig. 4c, which is located 0.67 chords downstream of the blade trailing edge. Values of C_w for each case appear in Table 1.

It can be seen in the table that all control configurations were capable of reducing the wake total pressure loss coefficient. Even though the cases for $D_c = 650.0$ were the most effective in this regard, no further details for these solutions will be presented here because of the high power requirements. Results of this comprehensive set of simulations will focus on the flowfields for $D_c = 25.0$, which proved to be the most effective with minimal power input.

Table 1 Description of cases

M_i	Re	Actuator device	Actuator type	Control direction	Actuator location	D_c	f^+	d	C_w
0.069	25,470	None	NA	NA	NA	NA	NA	NA	1.02
0.079	29,000	DBD	Pulsed	Counterflow	$x = 0.34$	25.0	7.56	50%	0.19
0.080	29,580	DBD	Continuous	Counterflow	$x = 0.34$	25.0	NA	NA	0.38
0.077	28,570	DBD	Pulsed	Coflow	$x = 0.37$	25.0	7.56	50%	0.46
0.071	26,330	DBD	Continuous	Coflow	$x = 0.37$	25.0	NA	NA	0.89
0.077	28,410	DBD	Pulsed	Counterflow	$x = 0.34$	25.0	3.78	50%	0.51
0.079	29,170	DBD	Pulsed	Counterflow	$x = 0.34$	25.0	7.56	25%	0.33
0.078	28,950	DBD	Pulsed	Coflow	$x = 0.37$	75.0	7.56	50%	0.12
0.074	27,250	DBD	Continuous	Coflow	$x = 0.37$	75.0	NA	NA	0.68
0.075	27,820	DBD	Pulsed	Coflow	$x = 0.37$	650.0	7.56	50%	0.01
0.074	27,610	DBD	Continuous	Coflow	$x = 0.37$	650.0	NA	NA	−0.06
0.081	29,950	Jet [28]	Pulsed	Spanwise	$x = 0.37$	NA	7.56	50%	0.48
0.079	29,100	Jet [28]	Continuous	Spanwise	$x = 0.37$	NA	NA	NA	0.52

Table 2 Mesh spacings with $D_c = 25.0, f^+ = 7.56$, and $d = 50\%$ for control cases

Actuator device	Actuator type	Control direction	$\Delta l^+_{\min}$	$\Delta l^+_{\max}$	$\Delta n^+_{\min}$	Δz^+
None	NA	NA	1.13	47.66	0.30	3.15
DBD	Pulsed	Counterflow	1.61	67.95	0.43	4.49
DBD	Continuous	Counterflow	1.03	43.16	0.27	2.85
DBD	Pulsed	Coflow	1.69	71.22	0.45	4.71
DBD	Continuous	Coflow	1.47	62.26	0.40	4.12

VI. Results for $D_c = 25.0$

This section describes results of simulations with $D_c = 25.0$. All of the pulsed cases considered here correspond to a frequency $f^+ = 7.56$ and a duty cycle d of 50%. Computational mesh spacings given in wall units for these cases are presented in Table 2. The reference condition for these spacings was taken as the wall shear of the time–mean solutions for the fully attached flow just upstream of separation.

A. Time–Mean Flowfields

Time–mean surface pressure coefficient distributions for the plasma-control and baseline (no control) cases are found in Fig. 6. In addition to temporal averaging, these distributions have also been averaged in the spanwise direction. The large plateau region in the baseline distribution is characteristic of a massively separated flow. Because of reduced blockage and increased inflow velocity, the effect of flow control is to decrease the pressure on the upstream portion of the suction surface, while increasing it downstream, relative to the baseline case. Continuous coflow control is seen to effect a minimal reduction of the plateau region. More significant benefits are obtained from continuous counterflow and pulsed coflow actuation, which reduced the length of the plateau by about 35%. The most effective control was produced by pulsed counterflow actuation that resulted in time–mean attached flow all the way to the blade trailing edge, thereby entirely eliminating the surface plateau in pressure.

Profiles of the time–mean velocity magnitude for the baseline and pulsed counterflow cases are found in Fig. 7. These profiles were extracted along lines (n) normal to the blade surface at each x station, on the periodic spanwise boundary. Magnitudes appearing in the figure have been normalized by the inflow velocity $\bar{q}_i$. Particularly notable is increased fullness of the control profile relative to the baseline solution near the trailing edge ($x = 0.9$).

A composite visual comparison of the flowfields for these cases is provided in Fig. 8. All time–mean results in this figure have also been averaged in the spanwise direction. Contours of u velocity are displayed in the top row of the figure, streamlines in the middle row, and pressure coefficient (C_p) at the bottom. Massive separation in the baseline case is apparent. Results indicated here are consistent with those observed in the surface pressure distributions (Fig. 6). Continuous coflow control had little effect on the size of the separated flow region, whereas both continuous counterflow and pulsed coflow actuation reduced its extent. This resulted in a narrower wake downstream of the blade, which decreased total pressure losses and lowered the value of C_w. Completely attached time–mean flow for pulsed counterflow control is evident in the figure.

Spanwise turbulent kinetic energy wave-number spectra are shown in Fig. 9. These spectra were generated along lines in the z direction at a distance of $n = 0.03$ from the blade surface. This length ($n = 0.03$) is approximately equal to one-half of the boundary-layer thickness of the time–mean velocity profile upstream of separation in the baseline case. At the most upstream station ($x = 0.5$), the energy of the flow with actuation is comparable to that beginning to evolve due to separation and transition in the baseline case. Further downstream ($x = 0.7$), actuation has resulted in greater turbulent kinetic energy, while near the trailing edge ($x = 0.9$) the situations are similar. It should be noted that these comparisons are

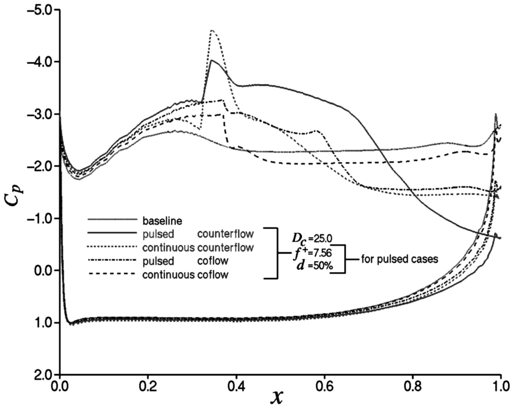

Fig. 6 Time–mean surface pressure coefficient distributions with $D_c = 25.0, f^+ = 7.56$, and $d = 50\%$ for pulsed cases.

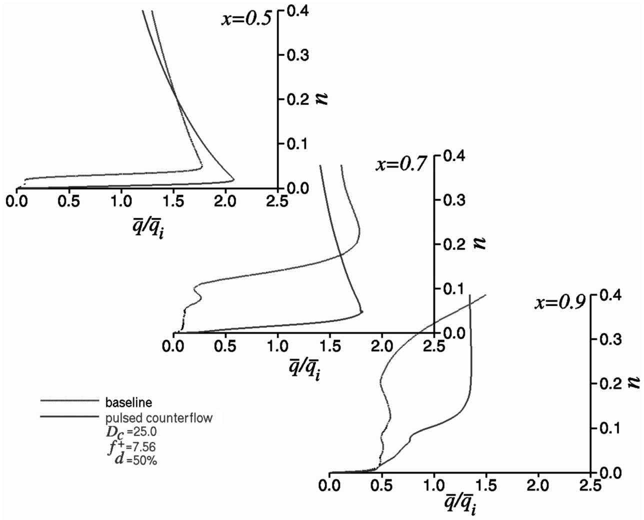

Fig. 7 Time–mean velocity magnitude profiles with $D_c = 25.0$, $f^+ = 7.56$, and $d = 50\%$.

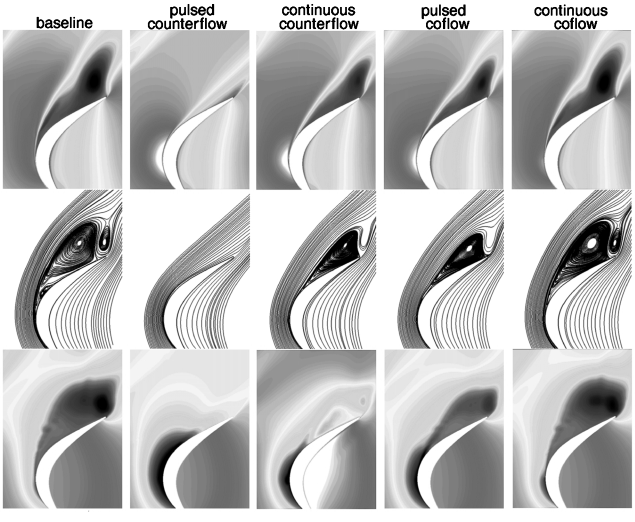

Fig. 8 Time–mean planar contours of u velocity, streamlines, and planar contours of C_p with $D_c = 25.0$, $f^+ = 7.56$, and $d = 50\%$ for pulsed cases.

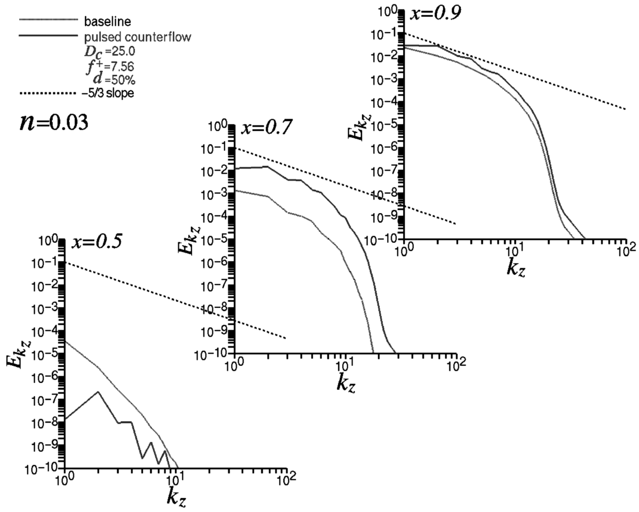

Fig. 9 Time–mean turbulent kinetic energy spanwise wave-number spectra with $D_c = 25.0, f^+ = 7.56$, and $d = 50\%$.

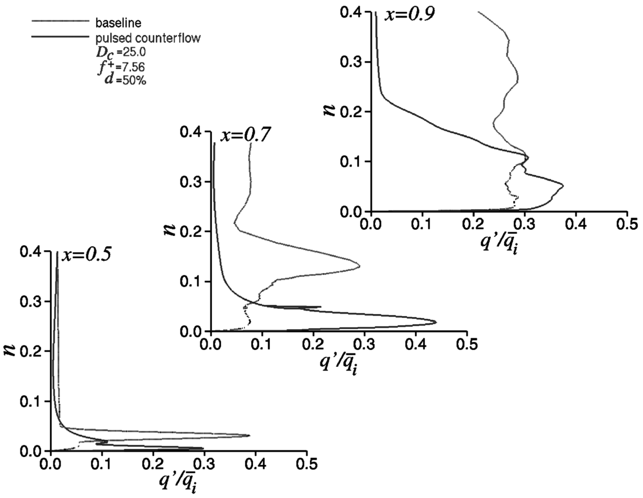

Fig. 10 Root-mean-square fluctuating velocity magnitude profiles with $D_c = 25.0, f^+ = 7.56$, and $d = 50\%$.

performed at a location very close to the blade surface. Further away, the total energy contained in the large structures of the massively separated region for the baseline case is very large. Because of the low Reynolds number of these flows, only a small portion of the spectrum at low wave number for $x = 0.9$ lies in the inertial range.

B. Unsteady Features of the Flowfields

Profiles of the root-mean-square fluctuating velocity magnitude at several steamwise locations are presented in Fig. 10. Fluctuations in the control case are related mostly to unsteadiness of the wall-mounted actuator, whereas those of the baseline flow evolve from unsteadiness of an unstable shear layer. As a result, the location of the maximum fluctuation occurs farther from the blade surface in the baseline solution. Although the peak fluctuating velocity magnitude for the control case is larger than that of the baseline for $x = 0.7$ and $x = 0.9$, actuation reduces high fluctuating velocity in the outer portion of the profile caused by massive separation.

A composite representation of the instantaneous flowfields for these cases is found in Fig. 11. Contours of u velocity and spanwise vorticity along the centerline plane appear in the top and middle rows of the figure, respectively, while spanwise vorticity on the blade surface viewed from above, is at the bottom. The middle row of spanwise vorticity is particularly useful for understanding the control mechanisms. Continuous coflow actuation at this low power level adds little energy to the dynamics of the flow. It does not create appreciable turbulent mixing in the near-wall region and does not affect the shear layer in the outer portion of the blade flowfield, which arises as the boundary layer separates. It is this shear layer that rolls up into a very large vortical structure, which is periodically shed near the trailing edge. Pulsed coflow actuation is somewhat more effective, even though less total energy is added. Because of inherent unsteadiness of the control device, mixing occurs in the boundary-layer region, which energizes it and facilitates maintaining attached flow. For the case of continuous counterflow actuation, the direction of the control force promotes a small local separation which enhances mixing and unsteadiness. This results in control effectiveness which is slightly better than that for the pulsed coflow case (see Table 1 for C_w). The situation for pulsed counterflow actuation is somewhat more complex and quite interesting. In this case, the control force direction not only generates small regions of local separation, but because of the pulsed application, these regions more readily convect downstream. This greatly strengthens the mixing processes. In addition, this type of actuation considerably modifies the structure of the unstable boundary layer. It forces the boundary layer to roll up into small vortices just downstream of the actuator location. These vortices are shed at a frequency one-half that of the pulsed control and convect downstream at a distance from the blade surface which is not large. This greatly enhances mixing and brings higher momentum fluid into the boundary layer, thereby maintaining time–mean attached flow and reducing wake losses. Dark portions of the surface vorticity (bottom row) correspond to regions of attached flow.

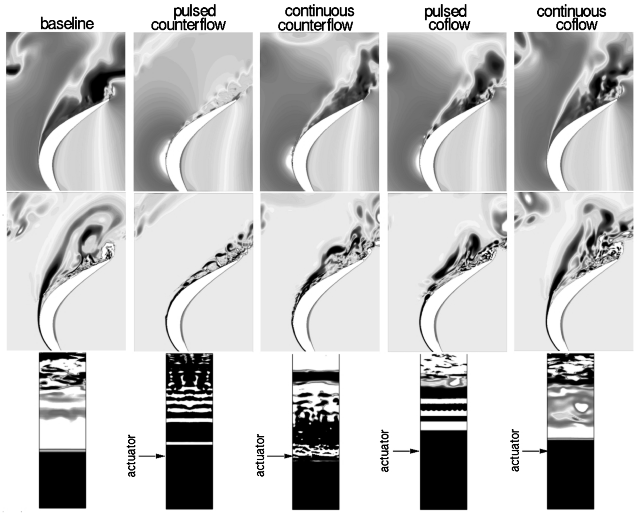

Fig. 11 Instantaneous planar contours of u velocity, planar contours of spanwise vorticity, and contours of spanwise vorticity on the blade surface with $D_c = 25.0, f^+ = 7.56$, and $d = 50\%$ for pulsed cases.

Provided in Fig. 12 are instantaneous streamlines at the blade midspan for pulsed counterflow actuation. Seen in the figure is the flowfield near the actuator location on the blade surface at four frames during the pulsing cycle. For $t/t_p = 0.0$, control has been inactive for one-half of the pulsing cycle, and the flow is attached. At $t/t_p = 0.2$, actuation has taken place for 20% of the cycle, creating a small separation bubble at the blade surface. By $t/t_p = 0.4$, the region of reversed flow has grown in size. Finally, when $t/t_p = 0.6$ the active portion of the cycle has ended, and the separation bubble begins to convect downstream.

Time histories of the nondimensional trailing-edge pressure are displayed in Fig. 13. The sizable excursions in the baseline case correspond to the shedding of large vortical structures. Because massive separation and the associated vortex shedding have been mitigated in the control case, the pressure fluctuations are greatly reduced.

Turbulent kinetic energy frequency spectra are shown in Fig. 14. The data used to generate these spectra were collected at $n = 0.03$, similar to that of Fig. 9. Near the actuator location $x = 0.5$, the

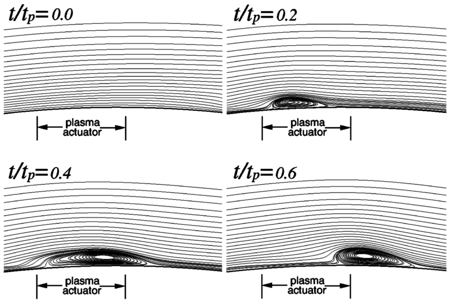

Fig. 12 Instantaneous streamlines at the midspan for pulsed counterflow actuation with $D_c = 25.0, f^+ = 7.56$, and $d = 50\%$.

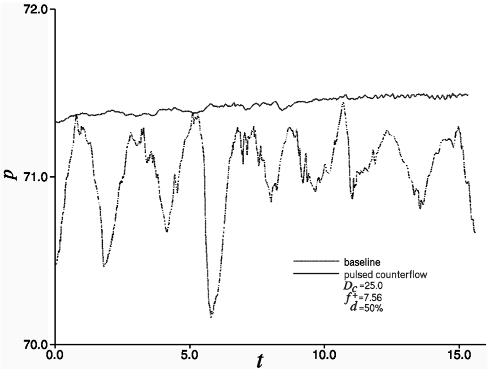

Fig. 13 Trailing-edge surface pressure time history for pulsed counterflow actuation with $D_c = 25.0, f^+ = 7.56$, and $d = 50\%$.

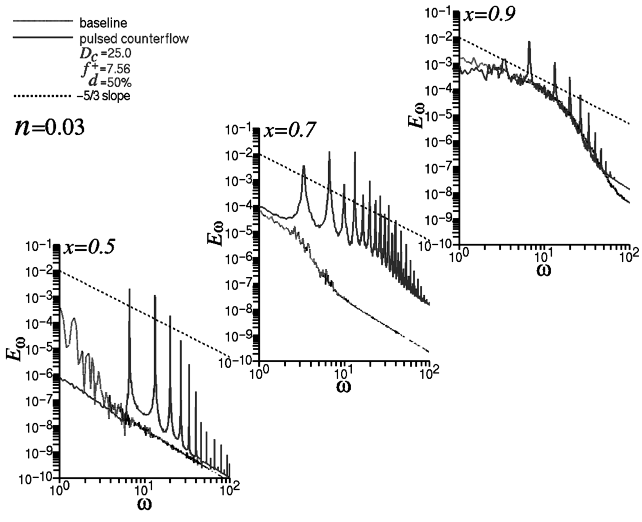

Fig. 14 Turbulent kinetic energy frequency spectra for pulsed counterflow actuation with $D_c = 25.0, f^+ = 7.56$, and $d = 50\%$.

discrete peaks in E_ω for the control case correspond to harmonics of the pulsing frequency. The occurrence of this behavior is identical to that for pulsed vortex-generating jets, which was described in detail in [28]. At $x = 0.7$ it is evident that subharmonics of the pulsing frequency have been excited. This phenomenon was caused by the small vortices generated in the boundary layer, downstream of the actuator, which was elucidated in Fig. 11. The energy of the control case at this location is larger than that of the baseline flow, but again it should be remembered that these spectra were taken close to the blade surface. Farther downstream in the trailing-edge region ($x = 0.9$), the respective spectra attain a similar level. The large peaks associated with actuation have diminished considerably, and a small inertial range is emerging.

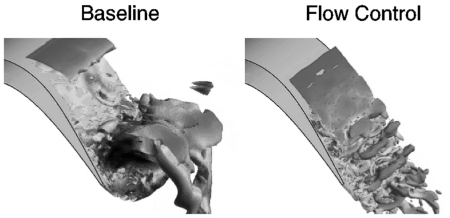

Fig. 15 Instantaneous isosurface of vorticity magnitude colored by u velocity for the baseline and pulsed counterflow actuation with $D_c = 25.0, f^+ = 7.56$, and $d = 50\%$.

A three-dimensional representation of the flow in the trailing-edge region is depicted in Fig. 15 by isosurfaces of vorticity magnitude, which have been colored by the u component of velocity. The value of the isosurfaces corresponds approximately to that at the edge of the shear layer upstream of separation. Both the vertical and the spanwise extents of the turbulent structures are visible for each solution. In the control case, these structures are initially coherent and quasi two dimensional, but eventually begin to break down as they convect downstream.

VII. Effect of Varying the Plasma-Induced Force

Effects of the magnitude of the plasma-induced body force were investigated by varying the value of the scale parameter D_c. As previously indicated, values as high as $D_c = 650.0$ were initially considered, but are thought to be unrealistic for practical plasma actuators. Time–mean surface pressure coefficient distributions for several values of D_c are presented in Fig. 16. These results were obtained during an early portion of the investigation, so that only coflowing actuation was used. Solutions for pulsed actuation were obtained for the nominal forcing frequency and duty cycle of $f^+ = 7.56$ and $d = 50\%$. The baseline distribution may be considered as the limiting case for $D_c = 0.0$. It is believed that power levels corresponding to $D_c = 75.0$ are fairly low and easily achievable by present plasma actuators. Continuous actuation for $D_c = 75.0$ and $D_c = 25.0$ is observed to exert little effect on massive separation and hence no reduction in the pressure plateau occurs. Consistent with previous results, pulsed actuation is seen to be much more effective in this regard. As expected, the higher value of D_c provides more control for both pulsed and continuous actuation. A quantitative assessment of the control effectiveness for each case can be found in terms of the wake total pressure loss coefficient C_w (see Table 1).

Features of the corresponding time–mean flowfields for these cases are exhibited in the composite comparison of Fig. 17. This representation is similar to that of previously discussed Fig. 8, where the top row is u, the middle row are streamlines, and the bottom row is C_p. Streamlines for continuous actuation with $D_c = 25.0$ demonstrate little control in that case. Some improvement of the

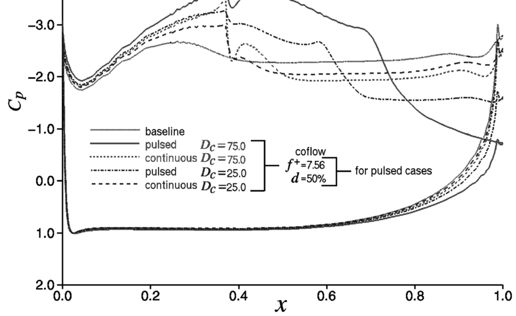

Fig. 16 Time–mean surface pressure coefficient distributions for coflow actuation with $f^+ = 7.56$ and $d = 50\%$ for pulsed cases.

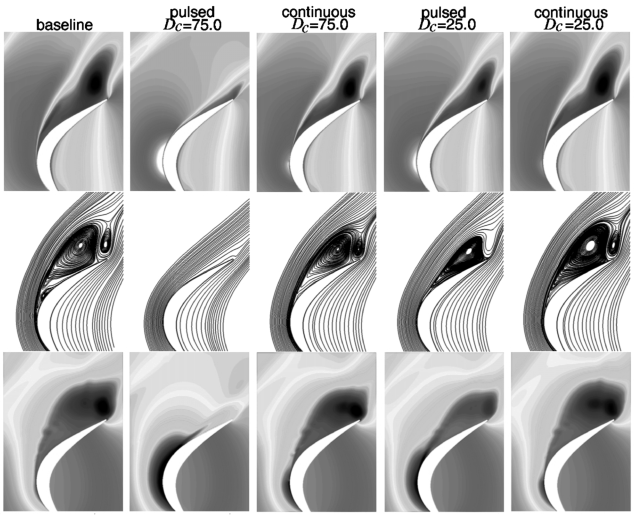

Fig. 17 Time–mean planar contours of u velocity, streamlines, and planar contours of C_p for coflow actuation with $f^+ = 7.56$ and $d = 50\%$ for pulsed cases.

baseline flow occurs for continuous actuation with $D_c = 75.0$, and appreciable control is exerted in the pulsed cases. It is evident that the time–mean flow remains attached virtually to the trailing edge for pulsed actuation with $D_c = 75.0$.

VIII. Effect of Varying the Pulsing Frequency

For pulsed counterflow actuation with $D_c = 25.0$ and a 50% duty cycle, a solution was obtained at a value of the forcing frequency equal to one-half the nominal value of $f^+ = 7.56$. Time–mean surface pressure coefficient distributions for both cases, along with that of the baseline, appear in Fig. 18. In the context of forcing frequency, we may consider the baseline flow to represent the limit situation for $f^+ = 0.0$. The figure indicates less effectiveness for the lower frequency $f^+ = 3.78$. This is probably because $f^+ = 3.78$ lies below a critical value, beyond which the control achieves its full effect. These results are consistent with the experiment of Huang et al. [10] who found similar behavior for coflowing control at a higher Reynolds number and smaller interblade spacing.

The composite comparison of the time–mean flowfields for these cases is provided in Fig. 19. As was shown previously (see Fig. 8), actuation with $f^+ = 7.56$ results in fully attached time–mean flow. With $f^+ = 3.78$, some mitigation of the massive separation is apparent.

IX. Effect of Varying the Duty Cycle

The effect of varying the duty was also examined for the case of pulsed counterflow actuation with $D_c = 25.0$. In addition to the 50% duty cycle case which has already been described, a solution was obtained for $d = 25\%$. Figure 20 displays the time–mean surface pressure coefficient distributions for these cases. Here, the baseline result corresponds to $d = 0\%$. Although the extent of the pressure plateau has been reduced with $d = 25\%$, control in this case was not as effective as that for $d = 50\%$. This is visually confirmed by the composite time–mean flowfields depicted in Fig. 21. These results illustrate that a minimum amount of input energy is required to exert effective control.

X. Discussion and Conclusions

The results presented here document numerical simulations that were performed to investigate the utility of plasma-based flow-control strategies for a transitional highly loaded low-pressure turbine. One of the main objectives of this effort was to identify effective actuation configurations, which possessed attainable minimal plasma-power requirements. The plasma scale parameter D_c was used to quantify these power requirements, and the wake total pressure loss coefficient C_w served as a metric for control efficiency. A simple phenomenological model was employed to represent plasma-induced body forces imparted by the actuator to the fluid field. On account of the transitional nature of the flowfield, a high-

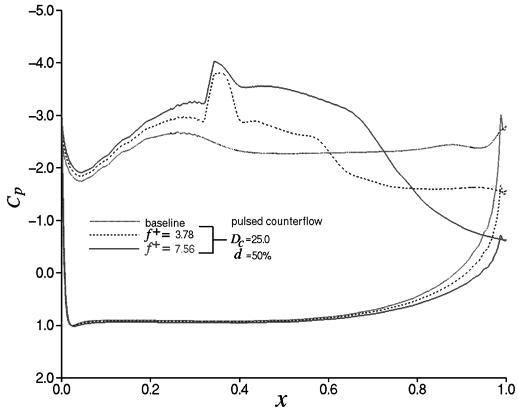

Fig. 18 Time–mean surface pressure coefficient distributions for pulsed counterflow actuation with $D_c = 25.0$ and $d = 50\%$.

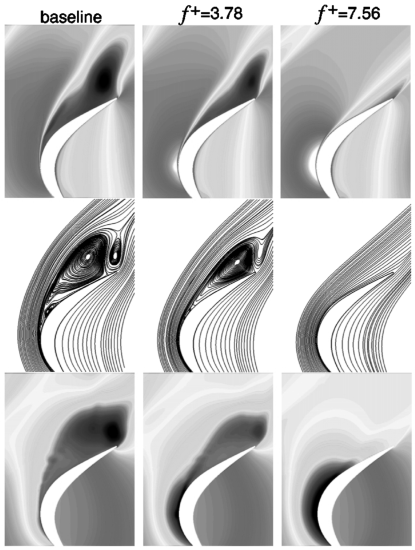

Fig. 19 Time–mean planar contours of u velocity, streamlines, and planar contours of C_p for pulsed counterflow actuation with $D_c = 25.0$ and $d = 50\%$.

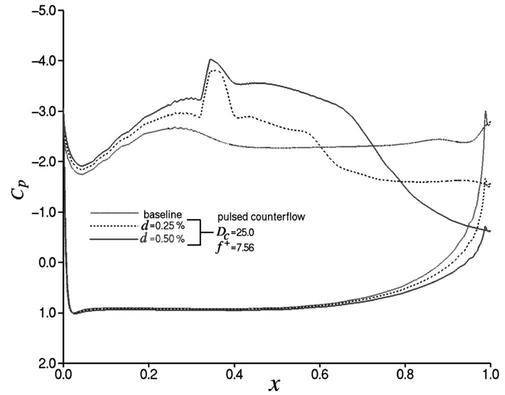

Fig. 20 Time–mean surface pressure coefficient distributions for pulsed counterflow actuation with $D_c = 25.0$ and $f^+ = 7.56$.

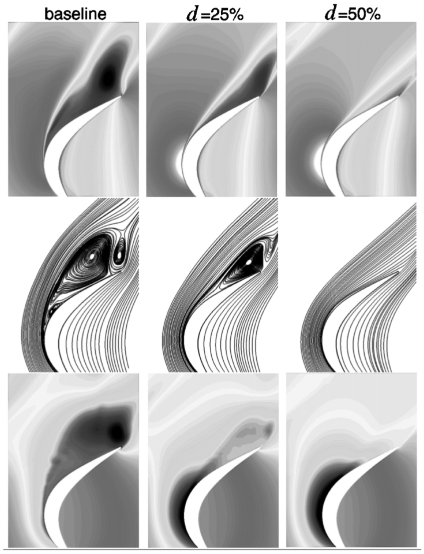

Fig. 21 Time–mean planar contours of u velocity, streamlines, and planar contours of C_p for pulsed counterflow actuation with $D_c = 25.0$ and $f^+ = 7.56$.

order numerical method with a locally refined region was used to capture the complex fluid behavior.

It should be noted that these computations correspond only to an isolated cascade configuration. As such, they neglect any heat input that would arise from the combustor in a practical turbine installation. This approach is identical to previous experimental [1–5] and computational [21–23,26–29] studies.

Solutions were obtained with both pulsed and continuous coflow actuation for $D_c = 650.0$, 75.0, and 25.0. In addition, the novel use of counterflow actuation was explored, and effects of frequency and duty cycle were considered, for low-power level requirements ($D_c = 25.0$). Generally it was found that higher power levels exerted greater control, as would be expected, and that a pulsed force application was more effective than continuous actuation. Because of its inherent tendency to enhance mixing, pulsing is an efficient control technique, even though it requires less power and imparts less energy to the flow than continuous actuation. In this regard, pulsed counterflow actuation with $D_c = 25.0$ for the frequency $f^+ = 7.56$ and a 50% duty cycle appeared to provide the most effective control with the least expenditure of energy. For that reason, this case has been described here in detail.

Although all the various actuator arrangements exerted some degree of control, the primary mechanisms by which this was achieved differ. For continuous coflowing actuation, momentum is added to the boundary layer in the near-wall region. This increases fullness of the boundary-layer profile, allowing it to overcome the adverse pressure gradient in the aft-blade region and maintain attached flow. Actuation of this type has been referred to as creating a jetlike flow along the blade surface [10]. Pulsed coflow actuation not only adds streamwise momentum, but also perturbs the highly unstable boundary layer near separation, resulting in the formation of vortical structures. These structures are fairly coherent in the spanwise direction close to their origin, owing to the full span actuator configuration. As these vortices convect downstream, high momentum fluid at the outer edge of the boundary layer is entrained and brought closer to the blade surface through rotation. These observations are in general agreement with the experimental findings of Huang et al. [10].

Both continuous and pulsed counterflow actuation are predicated upon perturbing the boundary layer to attain control benefits. Because the plasma force is opposing the flow direction in this situation, local separation occurs, resulting in vortex generation and turbulent mixing. With continuous counterflow actuation, the vortices that form are less coherent than those which occur for the pulsed case. That is why pulsed control is much more effective.

Because of fluid dynamic resonance with pulsed control, it could be expected that the vortex shedding frequency would synchronize with, and therefore be highly correlated to, that of the applied forcing. The exact nature of this correlation probably depends upon a number of factors including the streamwise extent of the actuator and the size of the separation bubble it produces (see Fig. 12), the thickness and state of the upstream boundary layer, and the time (or streamwise distance) required for vortex formation. In the pulsed counterflow case with $D_c = 25.0$, $f^+ = 7.56$, and $d = 50\%$, it required two pulsed forcing cycles to generate a single vortical structure. That is why the shedding frequency was one-half that of the forcing frequency (see Fig. 14).

Acknowledgments

The work presented here was sponsored by the U.S. Air Force Office of Scientific Research and was monitored by R. W. Jefferies. Computational resources were supported in part by a grant of supercomputer time from the U.S. Department of Defense Major Shared Resource Centers at Stennis Space Center, Mississippi, and Wright–Patterson AFB, Ohio. The authors are grateful to D. Gaitonde and J. Poggie for many helpful conversations.

References

[1] Sondergaard, R., Bons, J. P., Sucher, M., and Rivir, R. B., "Reducing Low-Pressure Turbine Stage Blade Count Using Vortex Generator Jet Separation Control," ASME Paper GT-2002-30602, June 2002.

[2] Bons, J. P., Sondergaard, R., and Rivir, R. B., "Control of Low-Pressure Turbine Separation Using Vortex Generator Jets," AIAA Paper 99-0367, Jan. 1999.

[3] Bons, J. P., Sondergaard, R., and Rivir, R. B., "Turbine Separation Control Using Pulsed Vortex Generator Jets," *Journal of Turbomachinery*, Vol. 123, No. 2, April 2001, pp. 198–206.

[4] Bons, J. P., Sondergaard, R., and Rivir, R. B., "The Fluid Dynamics of LPT Blade Separation Control Using Pulsed Jets," *Journal of Turbomachinery*, Vol. 124, No. 1, Jan. 2002, pp. 77–85.

[5] Sondergaard, R., Rivir, R. B., and Bons, J. P., "Control of Low-Pressure Turbine Separation Using Vortex Generator Jets," *Journal of Propulsion and Power*, Vol. 18, No. 4, July–Aug. 2002, pp. 889–895.

[6] List, J., Byerley, A. R., McLaughlin, T. E., and Dyken, R. D., "Using a Plasma Actuator to Control Laminar Separation on a Linear Cascade Turbine Blade," AIAA Paper 2003-1026, Jan. 2003.

[7] Huang, J., Corke, T. C., and Thomas, F. O., "Plasma Actuators for Separation Control of Low Pressure Turbine Blades," AIAA Paper 2003-1027, Jan. 2003.

[8] Corke, T. C., and Post, M. L., "Overview of Plasma Flow Control: Concepts, Optimization, and Applications," AIAA Paper 2005-0563, Jan. 2005.

[9] Huang, J., Corke, T. C., and Thomas, F. O., "Plasma Actuators for Separation Control of Low-Pressure Turbine Blades," *AIAA Journal*, Vol. 44, No. 1, Jan. 2006, pp. 51–57.

[10] Huang, J., Corke, T. C., and Thomas, F. O., "Unsteady Plasma Actuators for Separation Control of Low-Pressure Turbine Blades," *AIAA Journal*, Vol. 44, No. 7, July 2006, pp. 1477–1487.

[11] Lorber, P., McCormick, D., Anderson, T., Wake, D., MacMartin, D., Pollack, M., Corke, T., and Breuer, K., "Rotorcraft Retreating Blade Stall Control," AIAA Paper 2000-2475, June 2000.

[12] Corke, T. C., Jumper, E. J., Post, M. L., Orlov, D., and McLaughlin, T. E., "Application of Weakly-Ionized Plasmas as Wing Flow-Control Devices," AIAA Paper 2002-0350, Jan. 2002.

[13] Post, M. L., and Corke, T. C., "Separation Control on High Angle of Attack Airfoil Using Plasma Actuators," AIAA Paper 2003-1024, Jan. 2003.

[14] Post, M. L., and Corke, T. C., "Separation Control Using Plasma Actuators—Stationary and Oscillating Airfoils," AIAA Paper 2004-0841, Jan. 2004.

[15] Corke, T. C., He, C., and Patel, M. P., "Plasma Flaps and Slats: An Application of Weakly-Ionized Plasma Actuators," AIAA Paper 2004-2127, June–July 2004.

[16] Post, M. L., and Corke, T. C., "Separation Control Using Plasma Actuators—Dynamic Stall Control on an Oscillating Airfoil," AIAA Paper 2004-2517, June–July 2004.

[17] Morris, S. C., Corke, T. C., VanNess, D., Stephens, J., and Douville, T., "Tip Clearance Control Using Plasma Actuators," AIAA Paper 2005-0782, Jan. 2005.

[18] Thomas, F. O., Kozlov, A., and Corke, T. C., "Plasma Actuators for Bluff Body Flow Control," AIAA Paper 2006-2845, June 2006.

[19] Patel, M. P., Ng, T. T., Vasudevan, S., Corke, T. C., and He, C., "Plasma Actuators for Hingeless Aerodynamic Control of an Unmanned Air Vehicle," AIAA Paper 2006-3495, June 2006.

[20] Raverdy, B., Mary, I., Sagaut, P., and Liamis, N., "Large-Eddy Simulation of the Flow Around a Low Pressure Turbine Blade," *Direct and Large-Eddy Simulation IV*, ERCOFTAC Series Vol. 8, edited by B. J. Guerts, R. Friedrich, and O. Metais, Kluwer Academic Publishers, Dordrecht, The Netherlands, 2001, pp. 381–388.

[21] Mittal, R., Venkatasubramanian, S., and Najjar, F. M., "Large-Eddy Simulation of Flow Through a Low-Pressure Turbine Cascade," AIAA Paper 2001-2560, June 2001.

[22] Postl, D., Gross, A., and Fasel, H. F., "Numerical Investigation of Low-Pressure Turbine Blade Separation Control," AIAA Paper 2003-0614, Jan. 2003.

[23] Rizzetta, D. P., and Visbal, M. R., "Numerical Investigation of Transitional Flow Through a Low-Pressure Turbine Cascade," AIAA Paper 2003-3587, June 2003.

[24] Wissink, J. G., "DNS of Separating, Low-Reynolds Number Flow in a Turbine Cascade with Incoming Wakes," *International Journal of Heat and Fluid Flow*, Vol. 24, No. 4, Aug. 2003, pp. 626–635.

[25] Kalitzin, G., Wu, X., and Durbin, P. A., "DNS of Fully Turbulent Flow in a LPT Passage," *International Journal of Heat and Fluid Flow*, Vol. 24, No. 4, Aug. 2003, pp. 636–644.

[26] Postl, D., Gross, A., and Fasel, H. F., "Numerical Investigation of Active Flow Control for Low-Pressure Turbine Blade Separation," AIAA Paper 2004-0750, Jan. 2004.

[27] Gross, A., and Fasel, H. F., "Active Control of Separation for Low-Pressure Turbine Blades," AIAA Paper 2004-2203, June–July 2004.

[28] Rizzetta, D. P., and Visbal, M. R., "Numerical Study of Active Flow Control for a Transitional Highly-Loaded Low-Pressure Turbine," *Journal of Fluids Engineering*, Vol. 128, No. 5, Sept. 2006, pp. 956–967.

[29] Rizzetta, D. P., and Visbal, M. R., "Numerical Simulation of Separation Control for Transitional Highly-Loaded Low-Pressure Turbines," *AIAA Journal*, Vol. 43, No. 9, Sept. 2005, pp. 1958–1967.

[30] Visbal, M. R., Gaitonde, D. V., and Roy, S., "Control of Transitional and Turbulent Flows Using Plasma-Based Actuators," AIAA Paper 2006-3230, June 2006.

[31] Gaitonde, D. V., Visbal, M. R., and Roy, S., "Control of Flow Past a Wing Section with Plasma-Based Body Forces," AIAA Paper 2005-5302, June 2005.

[32] Visbal, M. R., and Gaitonde, D. V., "Control of Vortical Flows Using Simulated Plasma Actuators," AIAA Paper 2006-0505, Jan. 2005.

[33] Beam, R., and Warming, R., "An Implicit Factored Scheme for the Compressible Navier-Stokes Equations," *AIAA Journal*, Vol. 16, No. 4, April 1978, pp. 393–402.

[34] Gordnier, R. E., and Visbal, M. R., "Numerical Simulation of Delta-Wing Roll," AIAA Paper 93-0554, Jan. 1993.

[35] Jameson, A., Schmidt, W., and Turkel, E., "Numerical Solutions of the Euler Equations by Finite Volume Methods Using Runge-Kutta Time Stepping Schemes," AIAA Paper 81-1259, June 1981.

[36] Pulliam, T. H., and Chaussee, D. S., "A Diagonal Form of an Implicit Approximate-Factorization Algorithm," *Journal of Computational Physics*, Vol. 39, No. 2, Feb. 1981, pp. 347–363.

[37] Lele, S. A., "Compact Finite Dierence Schemes with Spectral-Like Resolution," *Journal of Computational Physics*, Vol. 103, No. 1, Nov. 1992, pp. 16–42.

[38] Visbal, M. R., and Gaitonde, D. V., "High-Order-Accurate Methods for Complex Unsteady Subsonic Flows," *AIAA Journal*, Vol. 37, No. 10, Oct. 1999, pp. 1231–1239.

[39] Gaitonde, D., Shang, J. S., and Young, J. L., "Practical Aspects of High-Order Accurate Finite-Volume Schemes for Electromagnetics," AIAA Paper 97-0363, Jan. 1997.

[40] Rizzetta, D. P., and Visbal, M. R., "Numerical Investigation of Plasma-Based Flow Control for a Transitional Highly-Loaded Low-Pressure Turbine," AIAA Paper 2007-938, Jan. 2007.

[41] Gaitonde, D., and Visbal, M. R., "High-Order Schemes for Navier-Stokes Equations: Algorithm and Implementation into FDL3DI," Air Force Research Laboratory, TR AFRL-VA-WP-TR-1998-3060, Wright–Patterson AFB, OH, Aug. 1998.

[42] Gordnier, R. E., and Visbal, M. R., "Numerical Simulation of Delta-Wing Roll," *Aerospace Science and Technology*, Vol. 2, No. 6, Sept. 1998, pp. 347–357.

[43] Gordnier, R. E., "Computation of Delta-Wing Roll Maneuvers," *Journal of Aircraft*, Vol. 32, No. 3, May 1995, pp. 486–492.

[44] Visbal, M. R., "Computational Study of Vortex Breakdown on a Pitching Delta Wing," AIAA Paper 93-2974, July 1993.

[45] Visbal, M., Gaitonde, D., and Gogineni, S., "Direct Numerical Simulation of a Forced Transitional Plane Wall Jet," AIAA Paper 98-2643, June 1998.

[46] Rizzetta, D. P., Visbal, M. R., and Stanek, M. J., "Numerical Investigation of Synthetic-Jet Flowfields," *AIAA Journal*, Vol. 37, No. 8, Aug. 1999, pp. 919–927.

[47] Rizzetta, D. P., Visbal, M. R., and Blaisdell, G. A., "A Time-Implicit High-Order Compact Differencing and Filtering Scheme for Large-Eddy Simulation," *International Journal for Numerical Methods in Fluids*, Vol. 42, No. 6, June 2003, pp. 665–693.

[48] Rizzetta, D. P., and Visbal, M. R., "Numerical Study of Active Flow Control for a Transitional Highly-Loaded Low-Pressure Turbine," AIAA Paper 2005-5020, June 2005.

[49] Rizzetta, D. P., and Visbal, M. R., "Application of Large-Eddy Simulation to Supersonic Compression Ramps," *AIAA Journal*, Vol. 40, No. 8, Aug. 2002, pp. 1574–1581.

[50] Rizzetta, D. P., Visbal, M. R., and Gaitonde, D. V., "Large-Eddy Simulation of Supersonic Compression-Ramp Flow by a High-Order Method," *AIAA Journal*, Vol. 39, No. 12, Dec. 2001, pp. 2283–2292.

[51] Rizzetta, D. P., and Visbal, M. R., "Large-Eddy Simulation of Supersonic Cavity Flowfields Including Flow Control," *AIAA Journal*, Vol. 41, No. 8, Aug. 2003, pp. 1452–1462.

[52] Roth, J. R., "Aerodynamic Flow Acceleration Using Paraelectric and Peristaltic Electrohydrodynamic Effects of a One Atmosphere Uniform Glow Discharge Plasma," *Physics of Plasmas*, Vol. 10, No. 5, May 2003, pp. 2117–2128.

[53] Roth, J. R., Sin, H., and Madham, R. C. M., "Flow Re-Attachment and Acceleration by Paraelectric and Peristaltic Electrohydrodynamic (EHD) Effects," AIAA Paper 2003-0531, Jan. 2003.

[54] Shyy, W., Jayaraman, B., and Anderson, A., "Modeling of Glow Discharge-Induced Fluid Dynamics," *Journal of Applied Physics*, Vol. 92, No. 11, Dec. 2002, pp. 6434–6443.

[55] Steinbrenner, J. P., Chawner, J. P., and Fouts, C. L., "The GRIDGEN 3D Multiple Block Grid Generation System, Volume II: User's Manual," Wright Research and Development Center, TR WRDC-TR-90-3022, Wright–Patterson AFB, OH, Feb. 1991.

[56] Gruber, B., and Carstens, V., "The Impact of Viscous Effects on the Aerodynamic Damping of Vibrating Transonic Compressor Blades—A Numerical Study," *Journal of Turbomachinery*, Vol. 123, No. 2, April 2001, pp. 409–417.

[57] Visbal, M. R., and Gaitonde, D. V., "Very High-Order Spatially Implicit Schemes for Computational Acoustics on Curvilinear Meshes," *Journal of Computational Acoustics*, Vol. 9, No. 4, Dec. 2001, pp. 1259–1286.

[58] Sherer, S. E., "Further Analysis of High-Order Overset Grid Method with Applications," AIAA Paper 2003-3839, June 2003.

[59] Suhs, N. E., Rogers, S. E., and Dietz, W. E., "PEGASUS 5: An Automated Preprocessor for Overset-Grid Computational Fluid Dynamics," *AIAA Journal*, Vol. 41, No. 6, June 2003, pp. 1037–1045.

[60] Message Passing Interface Forum, "MPI: A Message-Passing Interface Standard," University of Tennessee, Computer Science Department TR CS-94-230, Knoxville, TN, April 1994.

K. Powell
Associate Editor